Data Mine

SCENTAR: A High-Density Nodal Array to Study the Structure and Seismogenic Behavior of the Southern Cascadia Forearc

Jonathan R. Delph[*1], Amanda M. Thomas[2], A. Christian Stanciu[2,3], Khurram Aslam[2,4], Avigyan Chatterjee[2,5], and Vincent Sassard[1]

Abstract

Tectonic and seismogenic variations in subduction forearcs can be linked through various processes associated with subduction. Along the Cascadia forearc, significant variations between different geologic expressions of subduction appear to correlate, such as episodic tremor-and-slip (ETS) recurrence interval, intraslab seismicity, slab dip, uplift and exhumation rates, and topography, which allows for the systematic study of the plausible controlling mechanisms behind these variations. Even though the southern Cascadia forearc has the broadest topographic expression and shortest ETS recurrence intervals along the margin, it has been relatively underinstrumented with modern seismic equipment. Therefore, better seismic images are needed before robust comparisons with other portions of the forearc can be made. In March 2020, we deployed the Southern Cascadia Earthquake and Tectonics Array throughout the southern Cascadia forearc. This array consisted of 60 continuously recording three-component nodal seismometers with an average station spacing of ∼15 km, and stations recorded ∼38 days of data on average. We will analyze this newly collected nodal dataset to better image the structural characteristics and constrain the seismogenic behavior of the southern Cascadia forearc. The main goals of this project are to (1) constrain the precise location of the plate interface through seismic imaging and the analysis of seismicity, (2) characterize the lower crustal architecture of the overriding forearc crust to understand the role that this plays in enabling the high nonvolcanic tremor density and short episodic slow-slip recurrence intervals in the region, and (3) attempt to decouple the contributions of subduction versus San Andreas–related deformation to uplift along this particularly elevated portion of the Cascadia forearc. The results of this project will shed light on the controlling mechanisms behind heterogeneous ETS behavior and variable forearc surficial responses to subduction in Cascadia, with implications for other analogous subduction margins.

Cite this article as Delph, J. R., A. M. Thomas, A. C. Stanciu, K. Aslam, A. Chatterjee, and V. Sassard (2022). SCENTAR: A High-Density Nodal Array to Study the Structure and Seismogenic Behavior of the Southern Cascadia Forearc, *Seismol. Res. Lett.* **XX**, 1–11, doi: 10.1785/0220220251.

Supplemental Material

Introduction

Variations in the expression of subduction along convergent margins, such as surface topography, exhumation, structure, and seismogenic behavior, provide insight into the physical properties of the subduction interface. In particularly warm subduction zones, relatively shallow dehydration of the downgoing oceanic lithosphere (∼40 km; van Keken *et al.*, 2011) is also thought to contribute to these variations by enabling fluid-mediated seismogenic phenomena such as nonvolcanic tremor (NVT) and episodic slow slip based on seismic imaging (Shelly *et al.*, 2006; Audet *et al.*, 2009), tidal modulation (Nakata *et al.*, 2008; Rubinstein *et al.*, 2008), and correlations with the locations of metamorphic dehydration reactions (Peacock, 2009; Condit *et al.*, 2020). These fluids are particularly important for controlling the rheology of the plate interface through the metamorphic alteration of near-interface lithologies, and

1. Department of Earth, Atmospheric, and Planetary Sciences, Purdue University, West Lafayette, Indiana, U.S.A., https://orcid.org/0000-0002-3256-9301 (JRD); https://orcid.org/0000-0003-2615-1715 (VS); 2. Department of Earth Sciences, University of Oregon, Eugene, Oregon, U.S.A., https://orcid.org/0000-0002-8768-2432 (ACS); https://orcid.org/0000-0001-7422-6529 (AC); 3. Department of Geophysics, Sandia National Laboratories, Albuquerque, New Mexico, U.S.A.; 4. Extreme Event Solutions Research, Air Worldwide Inc., Boston, Massachusetts, U.S.A.; 5. Nevada Seismological Laboratory, University of Nevada, Reno, Nevada, U.S.A.

*Corresponding author: jdelph@purdue.edu

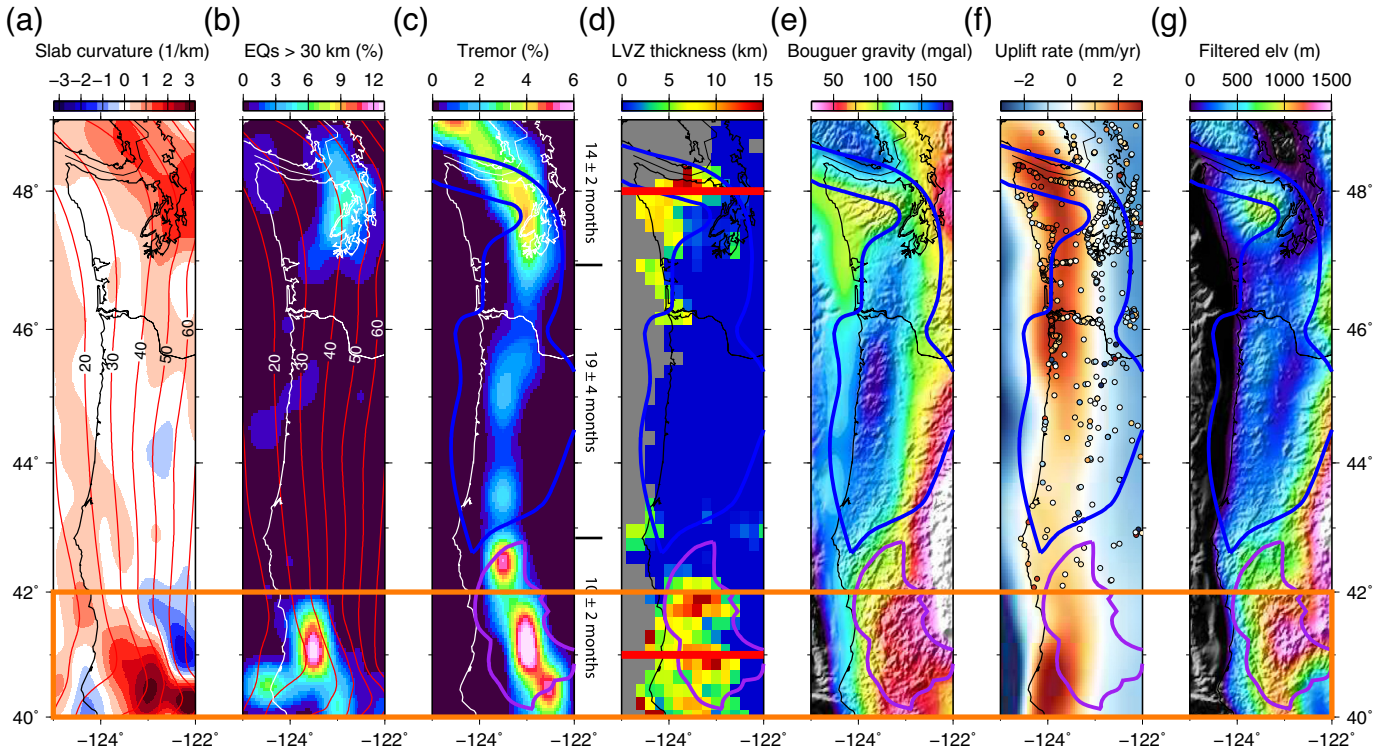

Figure 1. Map showing variable subduction characteristics along the Cascadia margin (after Delph *et al.*, 2021). Our local study will focus on the southern Cascadia margin (orange box), which shows (a) the highest slab curvature and shallowest slab dip; (b) the highest amounts of intraslab seismicity; (c) the highest density of nonvolcanic tremor (NVT) and shortest recurrence intervals for slow-slip events; (d) the largest crustal low shear-wave velocity zones; (e) the lowest Bouguer gravity anomalies; (f) the highest uplift rates; and (g) the highest topography along the entire Cascadia margin. Red lines in (d) indicate location of shear-velocity cross sections in Figure 2. Blue and purple polygons indicate boundaries for the Siletzia and Klamath terranes. The color version of this figure is available only in the electronic edition.

their presence has also been shown through numerical modeling to play a role in controlling efficiency of basal accretion ("subcretion") of material from the downgoing to overriding plate (Menant *et al.*, 2019). This in turn has a strong relationship with topographic growth, deformation, and exhumation in the overriding forearc (Menant *et al.*, 2020). Although these relationships can be predicted from thermopetrological and thermomechanical modeling, understanding their applicability to a subduction margin's structure and evolution requires a comparison between predictions and observed structures in the natural world.

The Cascadia margin of the northwestern United States is particularly well suited to test the interplay between numerical models, geophysical observables, and geologic and tectonic processes. Correlations between the surface expression of subduction and interplate seismogenic behavior have been linked to "subcretionary" processes using seismic imaging and other geophysical datasets (Fig. 1; Delph *et al.*, 2018, 2021). The case for this mechanism is most convincingly made along the northern portion of the Cascadia subduction zone, where an ~10–km-thick low shear-wave velocity zone (LVZ) with high internal reflectivity correlates with negative Bouguer gravity anomalies and has been interpreted as subcreted sedimentary material (Fig. 2; Calvert *et al.*, 2011; Delph *et al.*, 2018, 2021). Above and slightly trenchward of this LVZ is an elevated forearc accretionary complex (Olympic Mountains, Washington, U.S.A.), where clear domal uplift and exhumation are observed from low-temperature thermochronology and structural mapping (Brandon *et al.*, 1998), as would be predicted by the thermomechanical modeling of subcretion (Menant *et al.*, 2020). In addition, the observed velocities within these LVZs appear to necessitate the presence of free fluids and spatially correlate with NVT distribution along the margin (Delph *et al.*, 2018). The fluids are sourced from dehydration reactions in the downgoing oceanic crust based on thermopetrological modeling, which occurs over a similar depth range as slow slip (Condit *et al.*, 2020) indicating a strong link between fluids, subcretion, and surface uplift (Delph *et al.*, 2021).

The southern margin of Cascadia shows a strikingly similar surficial and shear-wave velocity structure to what is observed in northern Cascadia (Fig. 2); however, these features appear more exaggerated here than elsewhere along the margin. For instance, the seismogenic behavior of the southern Cascadia margin is characterized by the shortest recurrence intervals of episodic slow slip (Brudzinski and Allen, 2007), highest density of NVT (Wech, 2010), and large amounts of crustal and

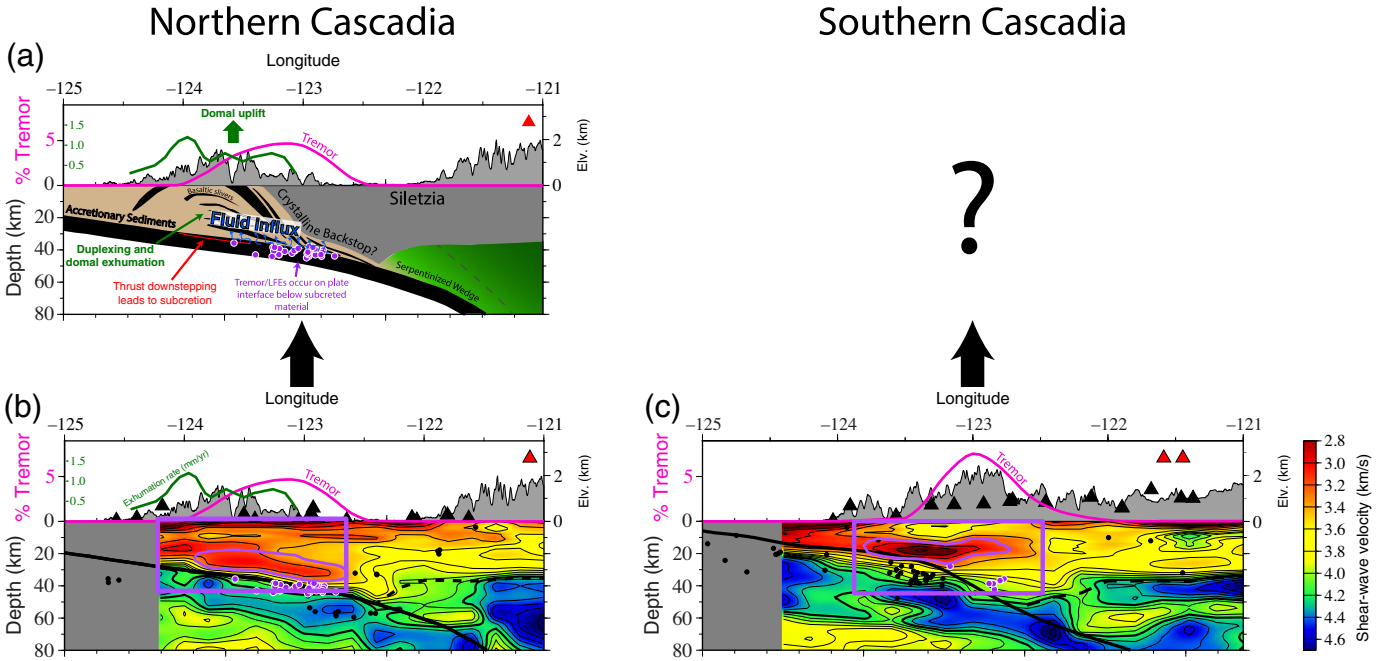

intraslab seismicity (McCrory *et al.*, 2012; Bostock *et al.*, 2019) compared with the rest of the margin. In addition, the broadly elevated forearc and high uplift rates cannot be adequately fit by models of plate locking (Kelsey *et al.*, 1994; Schmalzle *et al.*, 2014), implying a significant anelastic contribution to uplift. These characteristics make it tempting to invoke a similar "subcretion" hypothesis to what is interpreted farther north (Calvert *et al.*, 2011; Delph *et al.*, 2021). However, understanding whether subcretion plays a dominant role in controlling the intraplate seismicity of the overriding forearc and the surficial expression of subduction in southern Cascadia is complicated by (1) the lack of similar seismic reflection images to those in northern Cascadia (e.g., Calvert *et al.*, 2011), (2) an overriding plate of a different composition and architecture (intermediate composition Klamath terrane vs. the mafic composition Siletzia terrane in central and northern Cascadia), and (3) the combination of transpressional deformation related to the San Andreas system and subduction-related deformation.

To better understand the dominant controlling mechanisms behind southern Cascadia deformation patterns, surface expression, and seismogenic behavior, researchers at the University of Oregon and Purdue University deployed the Southern Cascadia Earthquake and Tectonics Array (SCENTAR), a passive array of 60 nodal seismometers in the southern Cascadia forearc. This array operated from early March to early April, 2020, and represents an approximately eightfold increase in station coverage compared with the permanent seismometer networks in the region over the deployment period (Fig. 3). This denser station spacing will allow for higher resolution images of the forearc crust immediately atop the locus of NVT and low-frequency earthquakes (purple polygon in Fig. 3) than can currently be obtained. The questions that this project aims to answer are

Figure 2. Forearc structure of northern and southern Cascadia. Location of cross sections shown in Figure 1d (red lines). In all images, purple dots represent low-frequency earthquakes, the purple polygon represents low-velocity zones interpreted to represent underplating material, the pink line above topography represents NVT distribution, the black triangles represent seismic stations, and the red triangles represent Holocene volcanic centers. (a) Conceptual cartoon of processes that are operating along the northern Cascadia margin (latitude: 48.0° N) based on thermochronology (green line; Brandon *et al.*, 1998), thermomechanical modeling (Menant *et al.*, 2019), and shear-wave velocity structure (as seen in panel b; Delph *et al.*, 2018). Figure after Delph *et al.* (2021). (b) Shear-wave velocity model (after Delph *et al.*, 2021). (c) Shear-wave velocity images of southern Cascadia (latitude: 41.0° N; after Delph *et al.*, 2021), showing a strikingly similar character to what is observed in northern Cascadia (b). The color version of this figure is available only in the electronic edition.

(1) what is the structure of the Cascadia forearc crust near the plate interface, and how might this relate to episodic slow slip and tremor, and (2) what allows for the very broad uplift of the southern Cascadia forearc? In addition, recent research has shown a rather significant discrepancy between low frequency earthquake (LFE) hypocenters and the location to the plate interface inferred from slab models and seismic images (Plourde *et al.*, 2015; Delph *et al.*, 2021), indicating a better model of the geometry and morphology of the plate interface in southern Cascadia is needed. To answer these questions, we integrate this dataset with both previously deployed and active seismic arrays operating in the region and perform *P*-wave receiver function analysis alongside LFE detection and location, ambient noise interferometry, and focal mechanism

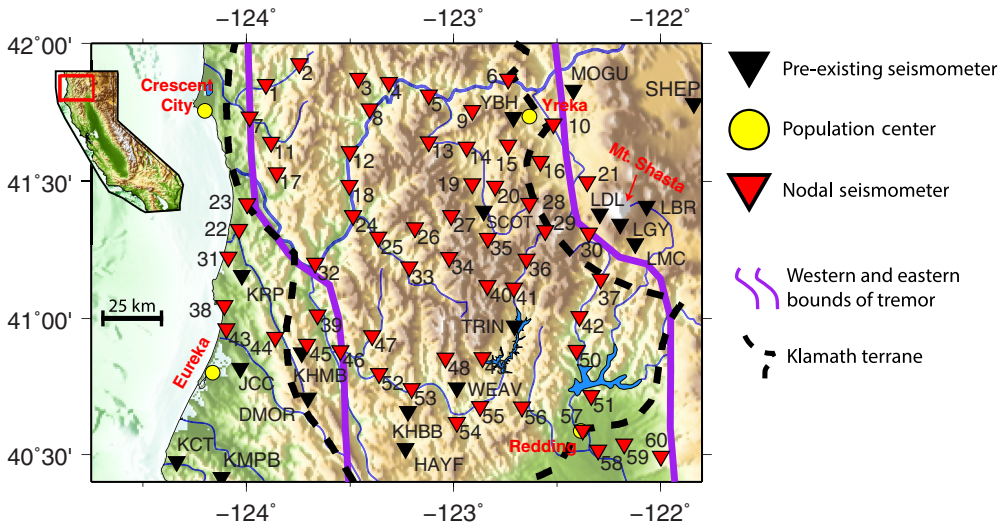

Figure 3. Nodal station locations (red triangles) deployed in the forearc of northern California. Black triangles are pre-existing broadband seismic stations belonging to the Northern California Seismic Network (NCSN network ID: BK). Purple boundaries mark edges of long-term NVT distribution in the area (from Wech, 2010 catalog; see Data and Resources). The black dashed line is approximate delineation of the Klamath terrane at the surface. The numbering system of nodal seismometers roughly increases from west-to-east and north-to-south. Note the location of Mt. Shasta. The color version of this figure is available only in the electronic edition.

analysis for small local earthquakes. We will also jointly invert the receiver function and ambient noise datasets to create a higher resolution 3D shear-wave velocity model of the region than currently exists.

Instrument Deployment and Details

This dataset consists of 60 Magseis Fairfield ZLand three-component 5 Hz nodal seismometers owned by the University of Oregon and managed by Dr. Amanda M. Thomas. Nodal seismometers are small, autonomous sensors with on-board digitizer, storage, and Global Positioning System (GPS) powered by a lithium-ion battery, allowing for the deployment of these units with trivial equipment in remote places. The instruments were deployed in early March 2020 in a gridded geometry over a 185 km (~40.5°–42° N) × 155 km (124.1°–122° E) area with ~15 km station spacing throughout the forearc of northern California specifically designed to lie immediately above the region of NVT (Fig. 3). The sampling rate for all stations was 250 Hz with a 12 dB gain. Station numbering increases from west to east and north to south. If possible, we used a posthole digger to make ~8 inch deep holes so that the nodal instrument could be buried ~1–2 inches below the surface to decrease noise (Farrell *et al.* 2018). All stations were coupled to the ground with a 4.6 inch metal spike (Fig. 4).

Most station locations were constrained to near state and interstate highways, covering a vast range of elevations from sea level to >2 km. Of the 60 stations, 30 were deployed on public land operated by the Klamath, Shasta-Trinity, and Six Rivers National Forests; two were deployed on the Hoopa Valley Indian Reservation; and the remaining were deployed on the properties of private landowners or adjacent to local roads. The original intent of this deployment was to swap the nodal instruments with fully charged nodals at the same locations after 1 month of operation to extend data recording, but complexities related to the COVID-19 pandemic prevented the second deployment of nodal instruments. Instead, stations were recovered in mid-April ~40 days after deployment so they could operate for their entire battery life and maximize data collection. The instruments recorded data for an average of ~38 days (Fig. 5). During this deployment, a cluster of seismicity occurred along the Mendocino Fracture Zone along with a slow-slip event whose southern edge overlapped with the array.

Overall Data Quality and Availability

Of the deployed 60 stations, 56 operated undisturbed for the entirety of the deployment. A consistent misorientation of ~10–20° east of north was observed during instrument removal, likely resulting from compass misalignment during deployment. Station orientations, dates of operation, and dates of disturbance to the best of the authors' knowledge are shown in Table S1, available in the supplemental material to this article. Four of the stations were severely disturbed during operation (stations 5, 48, 52, and 57). These sensors were removed from their deployed locations and either placed nearby on the ground (station 5) or replanted loosely with incorrect orientations (stations 48, 52, and 57). In addition, station 57 showed significantly higher amplitudes at high frequencies compared with other stations nearby, although the frequency content for data below 1 Hz appears similar; thus the data may still be useful albeit rather noisy. The date of disturbance was estimated from changes in the probabilistic power spectral density (PPSD) functions and spectrograms but is not known precisely.

Individual station noise was estimated using PPSDs over the entirety of the experiment (McNamara and Buland, 2004). PPSDs were calculated every 10 min with 5 min overlap following the approach of Lecocq *et al.* (2020) using the ObsPy package (Krischer *et al.*, 2015). Some examples are shown

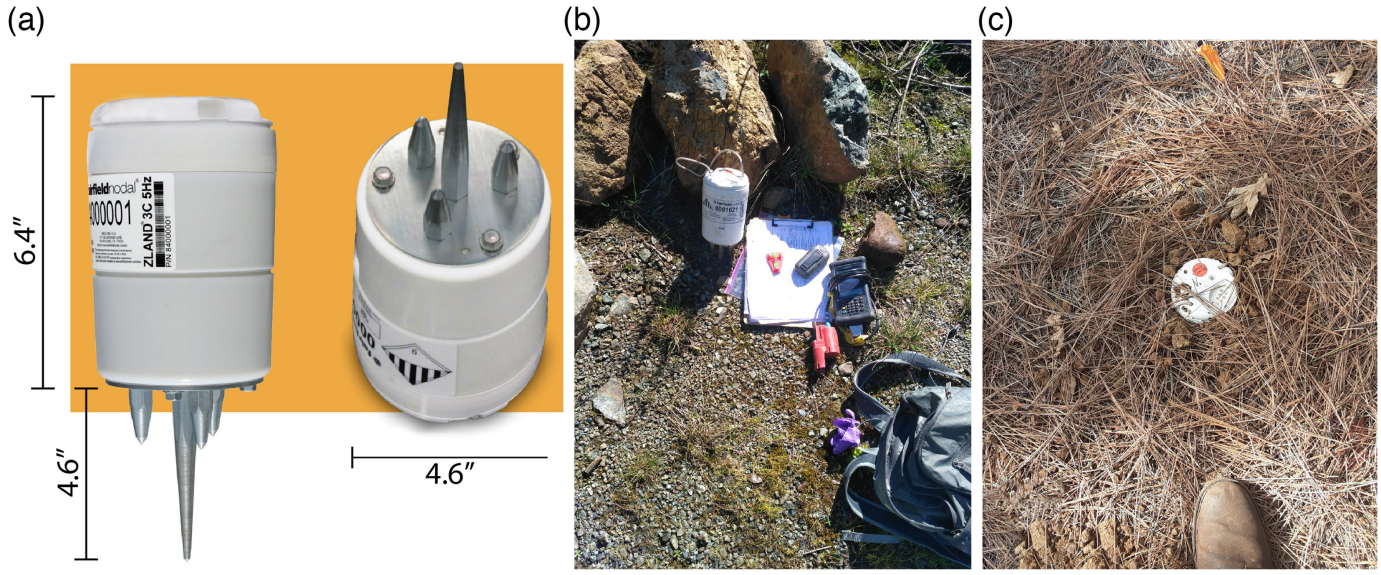

Figure 4. (a) Magseis Fairfield ZLand three-component nodal seismometer with dimensions (see Data and Resources). (b) The ZLand seismometer is readily deployed with a handheld deployment tool and terminal after preliminary experiment geometry is created using Magseis Fairfield's proprietary software. Compass (not shown) and bubble level are used to properly orient the instrument. Redundant Global Positioning System (GPS) locations were taken with a handheld GPS. (c) Typical example of an installation prior to complete burial (shoe for scale). Locations were marked with orange utility flags placed ~1 ft away from the instrument. The color version of this figure is available only in the electronic edition.

in Figure 6. Although these instruments have low-end corner frequency of 5 Hz, these instruments have been shown to accurately recover waveform character from teleseismic earthquakes at lower frequencies (<1 Hz) after instrument response removal, especially for large events (e.g., Wang *et al.*, 2019). Indeed, the PPSD plots generally show that ambient noise on the instruments for most stations do not cross the high noise model (HNM) until ~0.1 Hz (~10 s), consistent with previous estimations of noise on these instruments from other field deployments (e.g., Sweet *et al.*, 2018). This indicates that these data will be useful for understanding both local earthquakes characteristics and for analyzing teleseismic body waves, such as in receiver function analysis and teleseismic tomography, as has been demonstrated in previous studies (Ward and Lin, 2017; Ward *et al.*, 2018; Stanciu and Humphreys, 2021). Other studies have also shown that these instruments can recover ambient noise surface-wave measurements as well (e.g., Wang *et al.*, 2017, 2019), and there is no reason to believe this would not be the case with this array geometry. In fact, the quietest nodal stations show similar PPSDs to nearby broadband stations from ~0.1 to 10 Hz (red line, Fig. 6).

Initial Observations

To better understand the factors that affect data quality at our stations and how they might affect the analyses we propose to apply to these data, we inspected the regional characteristics of the PPSD signals in the array.

At frequencies generally used for teleseismic body-wave analysis (0.125–1 Hz; Fig. 7a), we see a change in the power of the noise spectrum that likely results from two main sources. The first dominant source is associated with the peak frequency of the secondary microseism (~6–8 s). Spectral noise trends in this frequency band show a decrease in power away from the coastline. This is expected because the main mechanism for generating the secondary microseismic energy arises from ocean-wave interactions in the ocean basins and (locally) with coastlines (Ardhuin *et al.*, 2011). There seems to be a local site response effect as well because stations located in the Franciscan terrane show higher noise levels, perhaps because of the strength of the bedrock. The Franciscan terrane comprises dominantly accretionary material (Hamilton, 1969), whereas the Klamath terrane bedrock is dominated by accreted crystalline oceanic and island arc material (Irwin, 1985).

At higher frequencies that overlap with local seismicity, low-frequency earthquakes, NVT (1–10 Hz; Fig. 7b), noise characteristics seem to be dominated by station proximity to human infrastructure, with secondary effects likely arising from site response. This is most strikingly seen near Redding, California, where all stations show high mean spectral power relative to more remote stations in the high elevations of the Klamath terrane (Fig. 7b). The generally higher noise levels also seem to run along the major highways, including the California coastal highway and Interstate-5, which are roughly demarcated by the north–south-trending westernmost and easternmost lines (red lines, Fig. 7). Juxtaposed on this signal, higher noise levels on proximal stations likely reflect small-

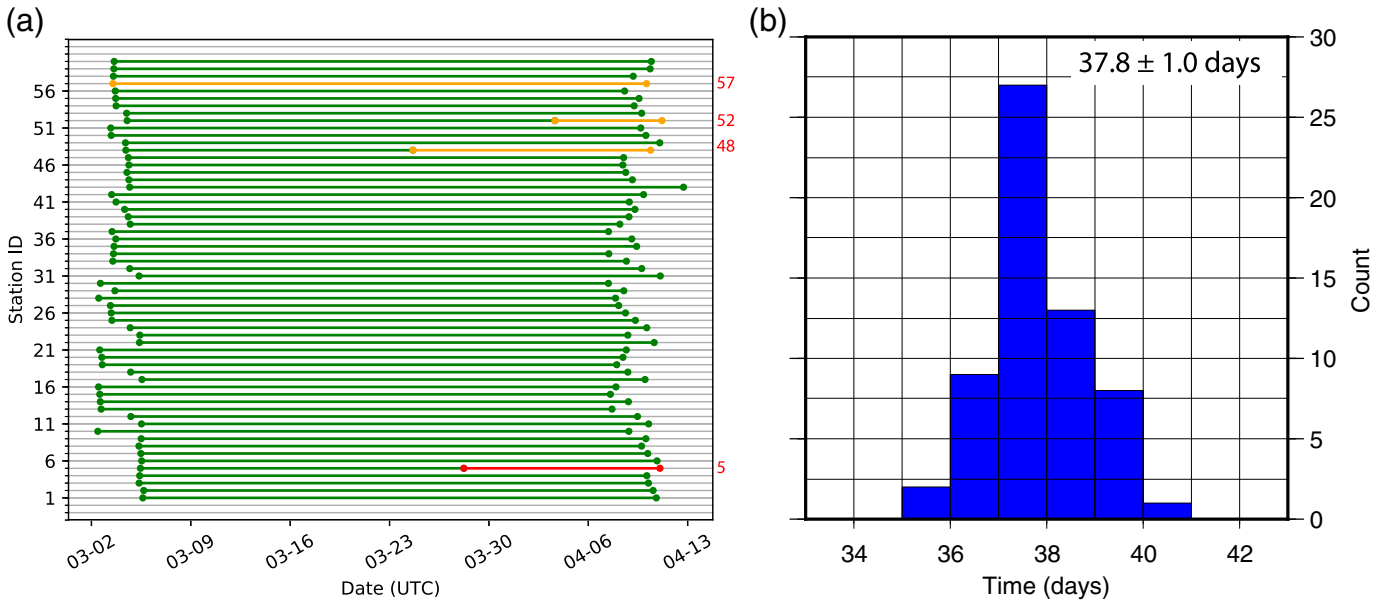

Figure 5. (a) Individual station operating time colored by known data quality. Green lines denote no known issues, orange lines denote disturbed station but useable data (with orientation change), and red line denotes unusable data. (b) Histogram of station operation duration. Seismometers were collecting at 250 samples per second. The color version of this figure is available only in the electronic edition.

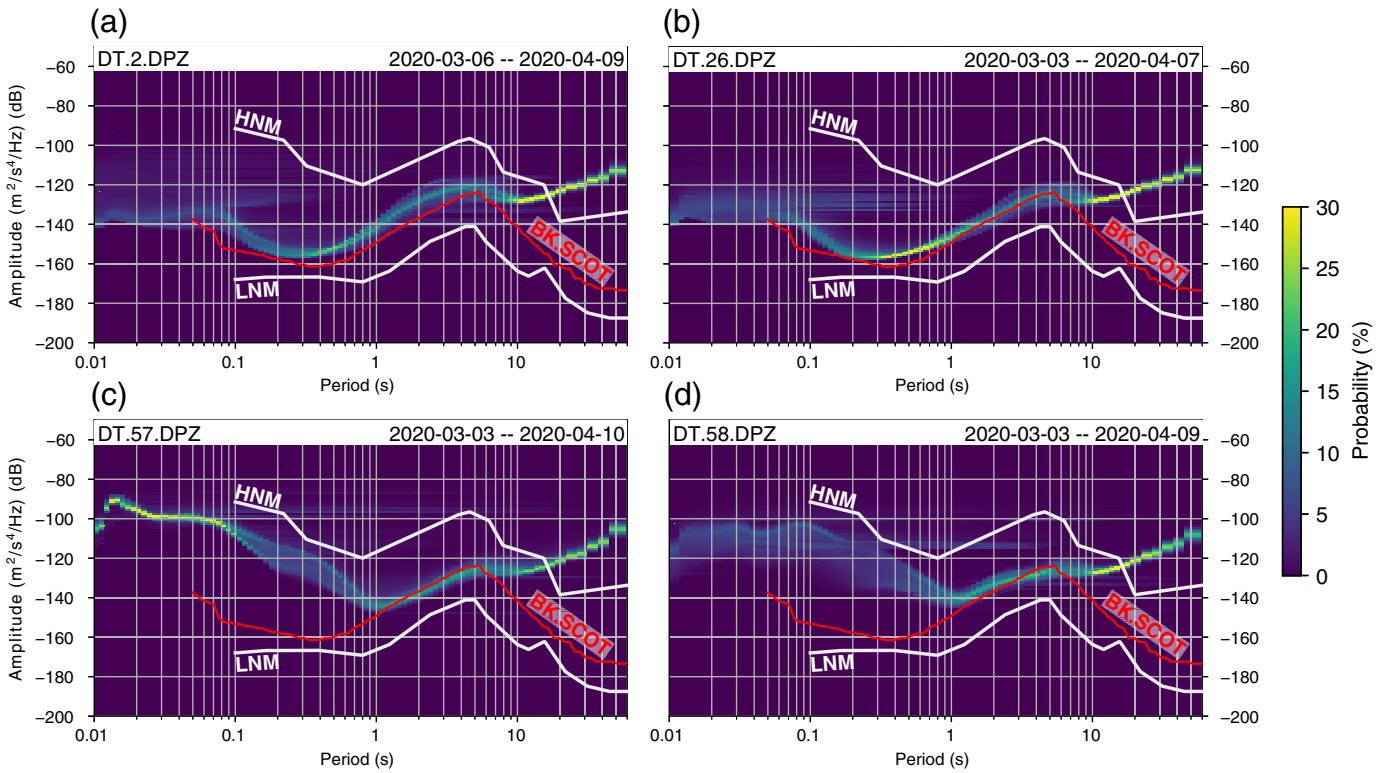

Figure 6. Probabilistic power spectral density (PPSD) plots for nodal stations. For comparison, the red line shows the noise level peak probability from a nearby broadband seismometer operated by the Northern California Seismic System (see Data and Resources) over the same time period. HNM, high noise model; LNM, low noise model (from Peterson, 1993). (a,b) PPSD plots for two "good"-quality stations located in the northwest and center of the array. (c,d) PPSD plots for seismometers located near the city of Redding, California. Higher noise levels at the high frequencies (1–10 Hz) likely result from anthropogenic sources. The color version of this figure is available only in the electronic edition.

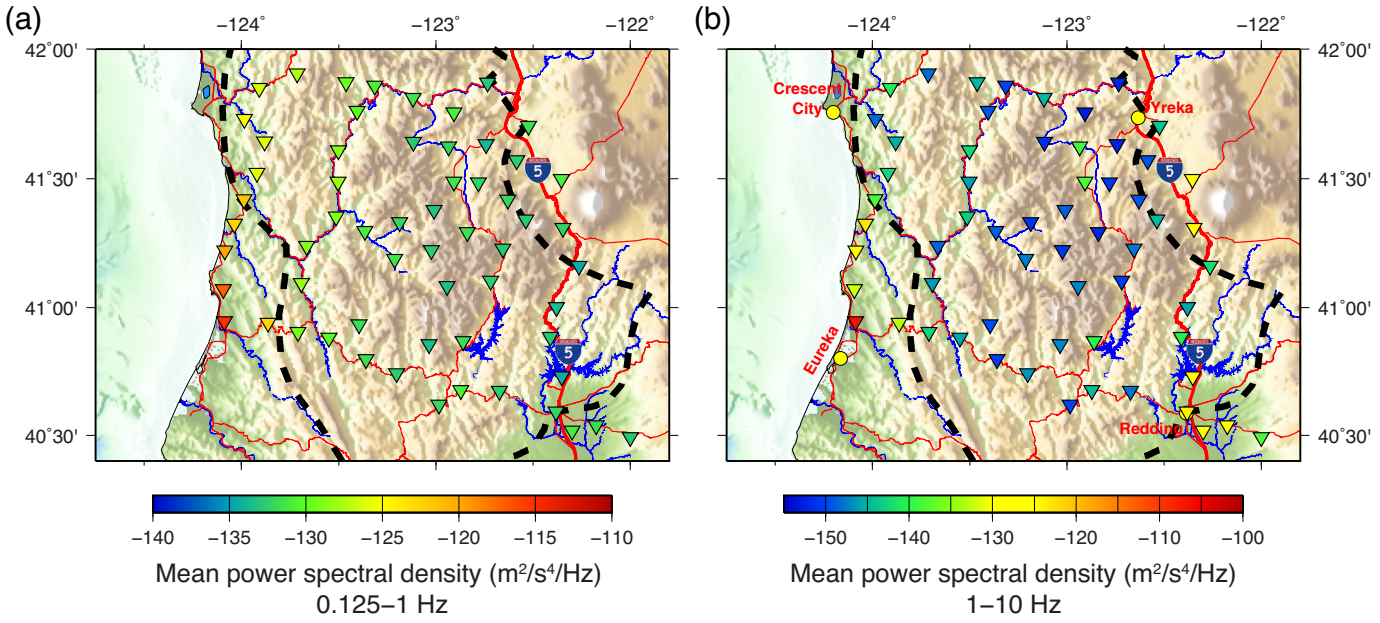

Figure 7. PPSD for each station over the duration of their operation for common frequency ranges used in (a) teleseismic and (b) local earthquake studies. The blue lines denote major river systems, black dashed line denotes Klamath Terrane boundaries, and the red lines denote major interstate and state highways. (a) At lower frequencies, mean seismic noise generally decreases with distance from the shoreline because the primary microseism band (~6–8 s) contributes to this noise level. (b) At high frequencies, increased noise levels generally correspond to locally generated anthropogenic noise (e.g., cities, highways) and river systems. Yellow circles denote major cities in study area. The color version of this figure is available only in the electronic edition.

scale shallow geological basins and waterways associated with the Klamath River and its tributaries (blue lines; Fig. 7b). Despite this deployment overlapping with COVID-19 shutdowns in the state of California on 19 March 2020, no significant decrease in the noise level of the data in this frequency band was observed on cursory inspection, which speaks to the remote nature of many of these stations.

Local and teleseismic events were clearly recorded on the seismic array during the period of operation and qualitatively compare well with nearby broadband seismometers from the Northern California Seismic Network (Figs. 8, 9). The high-frequency sensitivities of nodal seismometers make them particularly good for short-duration studies on local seismicity, but certain processing steps can also make them produce very comparable waveforms as broadband seismometers at intermediate periods (up to ~10 s). Thus, these nodal instruments can be used for both fine-scale local studies and as more traditional "broadband" seismic studies that utilize teleseismic earthquakes (as long as the signal-to-noise ratio of the teleseismic earthquakes is high enough).

Figure 8 shows an example of a local earthquake recorded on the array that occurred within the Gorda region of the Juan de Fuca plate. This M_L 3.5 event took place on 10 March 2020 and was clearly recorded on most of the stations in the array. We observe clear onsets for the *P* wave on most of the nodal stations (shown in black), whereas the *S*-wave arrival shows more variability, consistent with the broadband records (blue). Some of the nodal stations show quite a bit more noise prior to the *P*-wave onset compared to the broadband records, likely caused by differences in the deployment style (vaults for broadband vs. direct burial for nodal seismometers). Regardless, the clear arrivals on the nodal seismometers can be directly combined with those from the broadband stations in the region to understand travel-time variations. Furthermore, these waveforms can be used alongside nearby broadband stations for waveform modeling after the removal of the instrument response to make records comparable (e.g., Gong and McGuire, 2022).

Figure 9 shows an example of a *P*-wave and its coda from an M_w 7.5 teleseismic event recorded on the array that occurred on 25 March 2020 near the Kuril Islands compared with nearby broadband records. Given the large epicentral distance between the event and array, the *P* wave should look nearly identical on all records. Indeed, we observe very similar waveform characteristics between the event recorded on the broadband stations (blue traces) compared with the nodal records after the removal of the instrument response and filtering between 0.05 and 4 Hz (black). Many studies have used short-period (~1 Hz low corner) seismometers to compute *P*-wave receiver functions in the past (Niu *et al.*, 2005; Delph *et al.*, 2017), and this has been shown to work with 5 Hz nodal seismometers as well (e.g., Ward and Lin, 2017; Liu *et al.*, 2018; Lythgoe *et al.*, 2020). The only significant limitation in using nodal seismometers compared with seismometer systems at < 10 second periods is that the nodal seismometers are limited in their operation duration by their internal battery life,

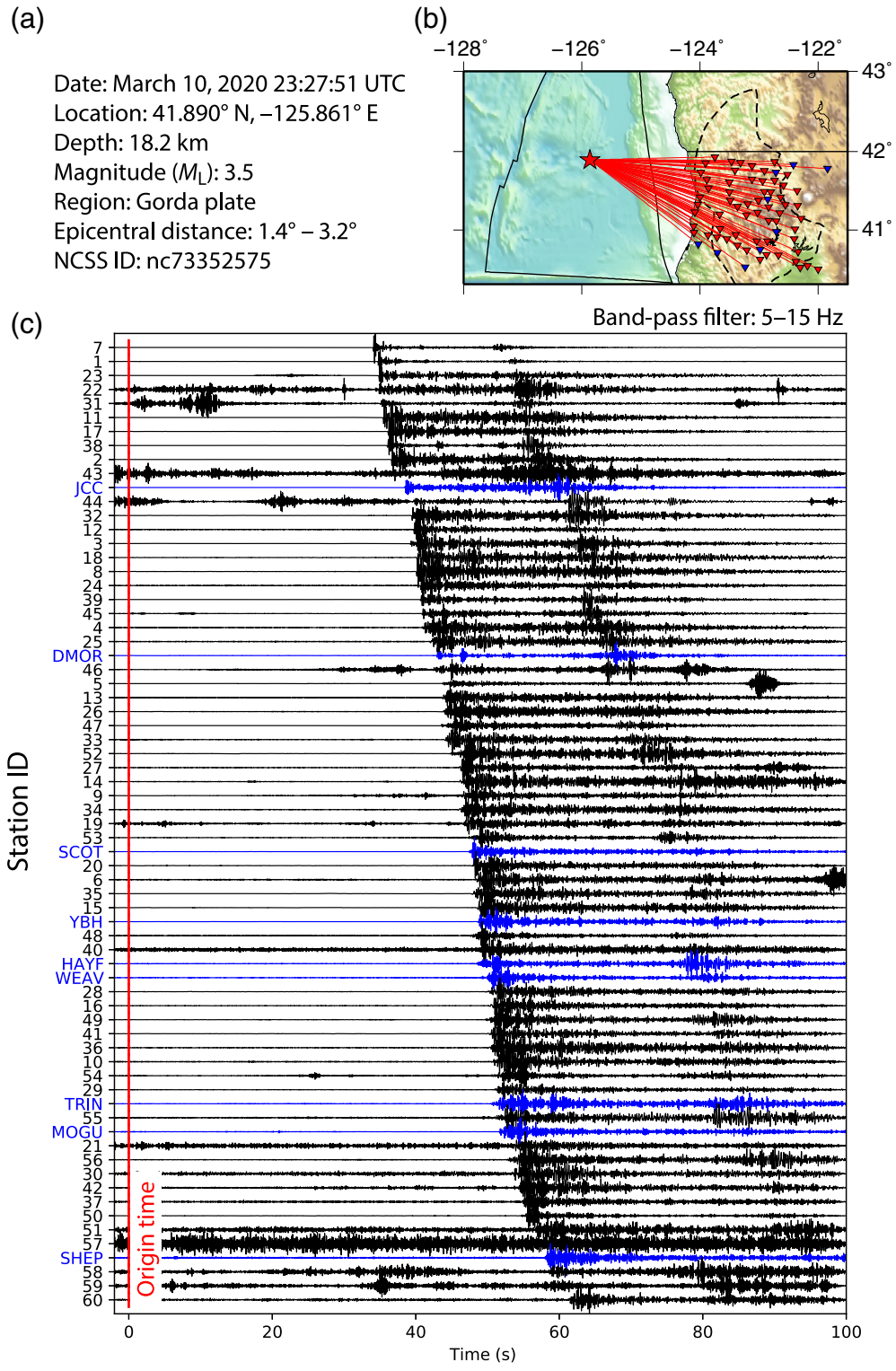

Figure 8. Data from a local earthquake recorded on Southern Cascadia Earthquake and Tectonics Array (SCENTAR) and nearby broadband stations. (a) Earthquake details. (b) Event location and great circle paths from event to SCENTAR stations (red) and Northern California Earthquake Data Center (NCEDC) broadband stations (blue). (c) Comparison of waveforms from nodal (black) and broadband (blue) seismometers. Stations are ordered by epicentral distance from the event. Clear *P*- and *S*-wave moveouts are apparent on most of the stations in the record section. Earthquake metadata from U.S. Geological Survey (USGS) National Earthquake Information Center (NEIC). The color version of this figure is available only in the electronic edition.

whereas other systems often operate with an external power supply. This can make targeted scattered-wave imaging studies using teleseismic waves somewhat risky because the quality of the results is generally dictated by the number of teleseismic events that occur over the duration of the deployment. During this deployment, the array recorded 19 teleseismic earthquakes amenable to typical *P*-wave receiver function calculation ($M_w > 5.5$, epicentral distances between 30° and 95°).

Our main goals for this dataset are to use a variety of techniques aimed at better imaging and characterizing the structure and seismicity of the southernmost Cascadia forearc, including using both teleseismic earthquakes alongside ambient noise methodologies to constrain the discontinuity and shear-wave velocity structure of the region and using machine learning techniques (e.g., Thomas *et al.*, 2021) to identify and characterize "traditional" seismicity and low-frequency earthquakes to understand the dominant state of stress in the overriding crust and better constrain the location and morphology of the plate interface. However, many other analyses can be done with this dataset. These include Love-wave ambient noise analysis (Lin *et al.*, 2008), constraining Rayleigh-wave anisotropy and horizontal-to-vertical ratios (e.g., Lin *et al.*, 2009; Lin and Schmandt, 2014), waveform modeling of the many Gorda plate earthquakes that took place over the duration of the deployment (e.g., Gong and McGuire, 2022), and calculating ground-motion predictions using horizontal-

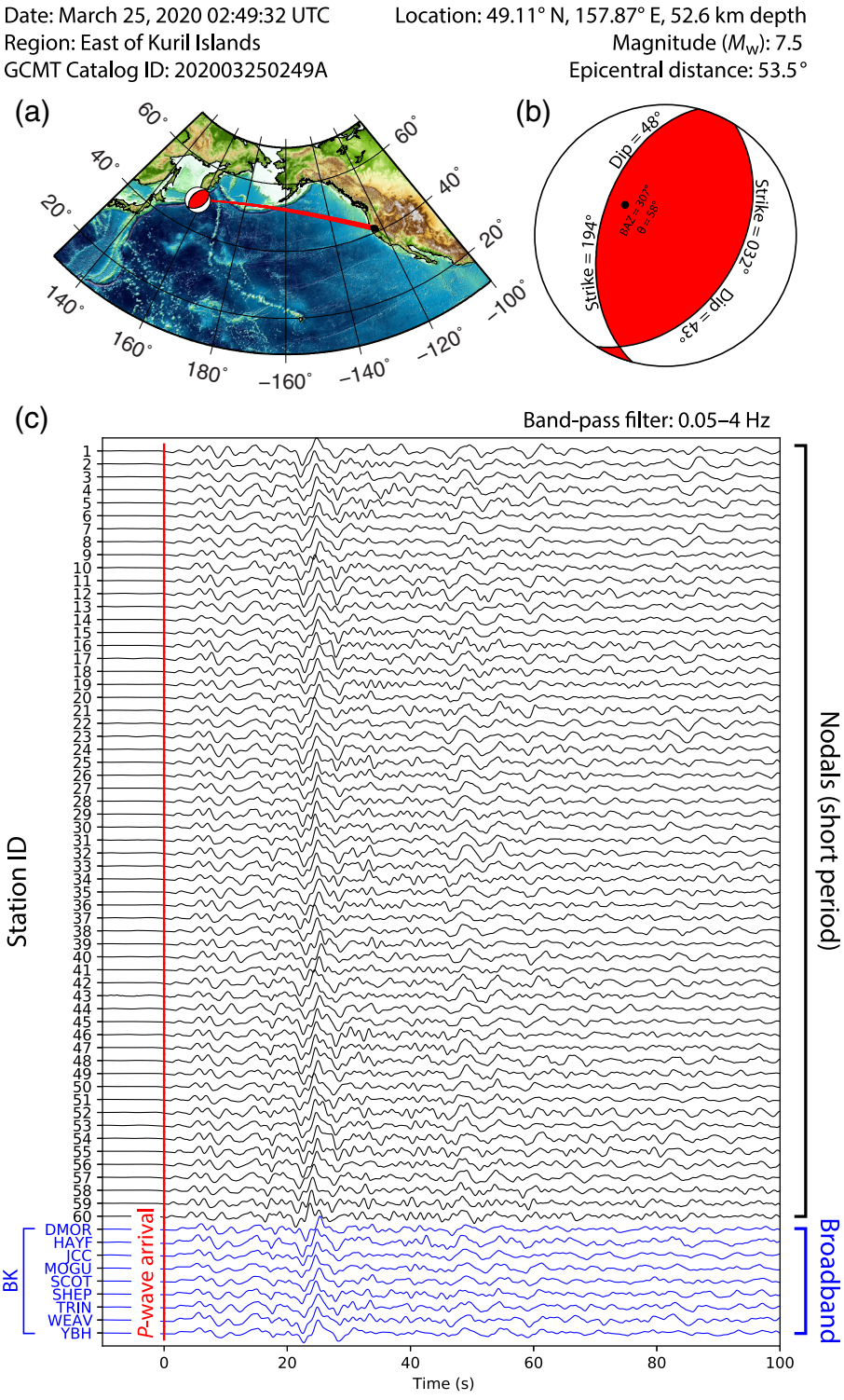

Figure 9. An example of data from a teleseismic earthquake recorded on the vertical component of SCENTAR and nearby broadband stations. Details for earthquake are shown at the top. (a) Location of event and great circle paths to the stations. (b) Focal mechanism of earthquake (Global Central Moment Tensor catalog; Ekström *et al.*, 2012). The black circle represents mean back azimuth and takeoff angle for the *P* wave on the focal mechanism stereonet. Low-amplitude, positive *P*-wave first-motion results from the array's position in a compressive quadrant near the nodal plane of the focal sphere. (c) Comparison of data from SCENTAR nodal stations (black traces) and NCEDC broadband instruments (blue traces). Earthquake metadata from USGS NEIC. The color version of this figure is available only in the electronic edition.

to-vertical spectral ratios or other site response analyses (e.g., Klimasewski *et al.*, 2019), which would also greatly contribute to the communal understanding of this portion of the Cascadia forearc.

Summary

The structural and rheological properties of a subduction margin directly influence seismogenesis and overriding plate deformation, but several aspects remain poorly understood. In early March 2020, the Southern Cascadia Earthquake and Tectonics Array (SCENTAR), consisting of 60 nodal seismic stations was deployed to investigate how the composition, structure, and seismic characteristics of the southern Cascadia margin contributes to broad uplift, topographic evolution, and high rates of episodic slow slip and tremor. To constrain the characteristics of the forearc, we will apply both robust and novel seismic methodologies, including (1) teleseismic receiver function imaging, (2) ambient noise interferometry, (3) a joint inversion of receiver functions and surface-wave dispersion measurements to obtain a new 3D shear-wave velocity model of the region, and (4) and seismicity analysis to understand the stress state of the southern Cascadia overriding plate and better constrain the morphology of the subduction interface. Insight into how these characteristics relate to the expression of subduction in southern Cascadia will then be used to better understand what controls variability in the manifestation of subduction elsewhere along the Cascadia margin. In

addition, these high-resolution images of forearc crustal structure will allow for the better understanding of the possible physical, compositional, and rheological controls on the processes of episodic tremor-and-slip.

Data and Resources

The Southern Cascadia Earthquake and Tectonics Array (SCENTAR) dataset was collected using funds provided through the University of Oregon and Purdue University, and these data will be analyzed as part of National Science Foundation (NSF) Grant Number 102939. SCENTAR data can be referenced by citing this article and its associate DOI (Delph and Thomas, 2020, doi: 10.7914/SN/3A_2020) and will be archived and made available through the Incorporated Research Institutions for Seismology Data Management Center (IRIS-DMC) after the completion of the NSF proposal (1 August 2024). Further information on station metadata is included in Table S1. Readers who are interested in obtaining this dataset ahead of the public release are encouraged to reach out to Jonathan Delph. Broadband data for comparison of local and teleseismic waveforms were obtained through the Northern California Earthquake Data Center (NCEDC; www.ncedc.org, last accessed February 2022). All maps were created using Generic Mapping Tools (GMT) version 5 (Wessel *et al.*, 2013). Data processing was performed using the ObsPy package (Krischer *et al.*, 2015). The information about Tremor map is available at www.pnsn.org/tremor (last accessed October 2022). The information about Magseis Fairfield is available at magseisfairfield.com (last accessed February 2020). The Northern California Seismic System is available at https://www.ncedc.org/ncss (last accessed October 2021).

Declaration of Competing Interests

The authors declare that there are no conflicts of interest recorded.

Acknowledgments

The authors thank numerous entities and private landowners for providing access to their land for the deployment of the nodal seismometers, including the Shasta-Trinity, Klamath, and Six Rivers National Forests, and in particular Jennifer Womack, Wendy Coats, and John Thornton. In addition, the authors thank Julia Cronin of Turtle Bay Exploration Park and Council chairman Byron Nelson of the Hoopa Valley Tribal Council and Indian Reservation. Broadband seismic data are available through the Northern California Earthquake Data Center (NCEDC, doi: 10.7932/NCEDC) as part of the Berkeley Digital Seismic Network (network BK: doi: 10.7932/BDSN).

References

Ardhuin, F., E. Stutzmann, M. Schimmel, and A. Mangeney (2011). Ocean wave sources of seismic noise, *J. Geophys. Res.* **116,** no. C9, doi: 10.1029/2011JC006952.

Audet, P., M. G. Bostock, N. I. Christensen, and S. M. Peacock (2009). Seismic evidence for overpressured subducted oceanic crust and megathrust fault sealing, *Nature* **457,** 76–78, doi: 10.1038/nature07650.

Bostock, M. G., N. I. Christensen, and S. M. Peacock (2019). Seismicity in Cascadia, *Lithos* **332/333,**55–66, doi: 10.1016/j.lithos.2019.02.019.

Brandon, M. T., M. K. Roden-Tice, and J. I. Carver (1998). Late Cenozoic exhumation of the Cascadia accretionary wedge in the Olympic Mountains, northwest Washington State, *GSA Bull.* **110,** 985–1009.

Brudzinski, M. R., and R. M. Allen (2007). Segmentation in episodic tremor and slip all along Cascadia, *Geology* **35,** 907–910, doi: 10.1130/G23740A.1.

Calvert, A. J., L. A. Preston, and A. M. Farahbod (2011). Sedimentary underplating at the Cascadia mantle-wedge corner revealed by seismic imaging, *Nature Geosci.* **4,** 545–548, doi: 10.1038/ngeo1195.

Condit, C. B., V. E. Guevara, J. R. Delph, and M. E. French (2020). Slab dehydration in warm subduction zones at depths of episodic slip and tremor, *Earth Planet. Sci. Lett.* **552,** 116601, doi: 10.1016/j.epsl.2020.116601.

Delph, J. R., and A. M. Thomas (2020). Southern Cascadia earthquake and tectonics array [Data Set], *Int. Fed. Digit. Seismogr. Networks*, doi: 10.7914/SN/3A_2020.

Delph, J. R., A. Levander, and F. Niu (2018). Fluid controls on the heterogeneous seismic characteristics of the Cascadia Margin, *Geophys. Res. Lett.* **45,** 11,021–11,029, doi: 10.1029/2018GL079518.

Delph, J. R., A. M. Thomas, and A. Levander (2021). Subcretionary tectonics: Linking variability in the expression of subduction along the Cascadia forearc, *Earth Planet. Sci. Lett.* **556,** 116724, doi: 10.1016/j.epsl.2020.116724.

Delph, J. R., K. M. Ward, G. Zandt, M. N. Ducea, and S. L. Beck (2017). Imaging a magma plumbing system from MASH zone to magma reservoir, *Earth Planet. Sci. Lett.* **457,**313–324, doi: 10.1016/j.epsl.2016.10.008.

Ekström, G., M. Nettles, and A. M. Dziewoński (2012). The global CMT project 2004–2010: Centroid-moment tensors for 13,017 earthquakes, *Phys. Earth Planet. In.* **200/201,** 1–9, doi: 10.1016/j.pepi.2012.04.002.

Farrell, J., S. Wu, K. M. Ward, and F. Lin (2018). Persistent noise signal in the FairfieldNodal three-component 5-Hz geophones, *Seismol. Res. Lett.* **89,** 1609–1617, doi: 10.1785/0220180073.

Gong, J., and J. J. McGuire (2022). Waveform signatures of earthquakes located close to the subducted Gorda plate interface, *Bull. Seismol. Soc. Am.* doi: 10.1785/0120210261.

Hamilton, W. (1969). Mesozoic California and the underflow of Pacific Mantle, *GSA Bull.* **80,** 2409–2430.

Irwin, W. P. (1985). Age and tectonics of plutonic belts in accreted Terranes of the Klamath Mountains, California and Oregon, in *Tectonostratigraphic Terranes of the Circum-Pacific Region*, D. G. Howell (Editor), Vol. 1, Circum-Pacific Council for Energy and Mineral Resources, Houston, Texas, Earth Science Series, 187–199.

Kelsey, H. M., D. C. Engebretson, C. E. Mitchell, and R. L. Ticknor (1994). Topographic form of the Coast Ranges of the Cascadia margin in relation to coastal uplift rates and plate subduction, *J. Geophys. Res.* **99,** doi: 10.1029/93jb03236.

Klimasewski, A., V. Sahakian, A. Baltay, J. Boatwright, J. B. Fletcher, and L. M. Baker (2019). κ0 and broadband site spectra in southern California from source model-constrained inversion, *Bull. Seismol. Soc. Am.* **109,** 1878–1889, doi: 10.1785/0120190037.

Krischer, L., T. Megies, R. Barsch, M. Beyreuther, T. Lecocq, C. Caudron, and J. Wassermann (2015). ObsPy: A bridge for seismology into the scientific Python ecosystem, *Comput. Sci. Discov.* **8,** 014003, doi: 10.1088/1749-4699/8/1/014003.

Lecocq, T., S. P. Hicks, K. Van Noten, K. van Wijk, P. Koelemeijer, R. S. M. De Plaen, F. Massin, G. Hillers, R. E. Anthony, M. Apoloner, *et al.* (2020). Global quieting of high-frequency seismic noise due to COVID-19 pandemic lockdown measures, *Science* **369,** 1338–1343, doi: 10.1126/science.abd2438.

Lin, F. C., and B. Schmandt (2014). Upper crustal azimuthal anisotropy across the contiguous U.S. determined by Rayleigh wave ellipticity, *Geophys. Res. Lett.* **41,** 8301–8307, doi: 10.1002/2014GL062362.

Lin, F. C., M. P. Moschetti, and M. H. Ritzwoller (2008). Surface wave tomography of the western United States from ambient seismic noise: Rayleigh and Love wave phase velocity maps, *Geophys. J. Int.* **173,** 281–298, doi: 10.1111/j.1365-246X.2008.03720.x.

Lin, F. C., M. H. Ritzwoller, and R. Snieder (2009). Eikonal tomography: Surface wave tomography by phase front tracking across a regional broad-band seismic array, *Geophys. J. Int.* **177,** 1091–1110, doi: 10.1111/j.1365-246X.2009.04105.x.

Liu, G., P. Persaud, and R. W. Clayton (2018). Structure of the northern Los Angeles basins revealed in teleseismic receiver functions from short-term nodal seismic arrays, *Seismol. Res. Lett.* **89,** 1680–1689, doi: 10.1785/0220180071.

Lythgoe, K. H., M. Ong Su Qing, and S. Wei (2020). Large-scale crustal structure beneath Singapore using receiver functions from a dense urban nodal array, *Geophys. Res. Lett.* **47,** doi: 10.1029/2020GL087233.

McCrory, P. A., J. L. Blair, F. Waldhauser, and D. H. Oppenheimer (2012). Juan de Fuca slab geometry and its relation to Wadati-Benioff zone seismicity, *J. Geophys. Res.* **117,** 1–24, doi: 10.1029/2012JB009407.

McNamara, D. E., and R. P. Buland (2004). Ambient noise levels in the continental United States, *Bull. Seismol. Soc. Am.* **94,** 1517–1527, doi: 10.1785/012003001.

Menant, A., S. Angiboust, and T. Gerya (2019). Stress-driven fluid flow controls long-term megathrust strength and deep accretionary dynamics, *Sci. Rep.* **9,** 1–11, doi: 10.1038/s41598-019-46191-y.

Menant, A., S. Angiboust, T. Gerya, R. Lacassin, M. Simoes, and R. Grandin (2020). Transient stripping of subducting slabs controls periodic forearc uplift, *Nat. Commun.* **11,** 1823, doi: 10.1038/s41467-020-15580-7.

Nakata, R., N. Suda, and H. Tsuruoka (2008). Non-volcanic tremor resulting from the combined effect of Earth tides and slow slip events, *Nature Geosci.* **1,** 676–678, doi: 10.1038/ngeo288.

Niu, F., A. Levander, S. Ham, and M. Obayashi (2005). Mapping the subducting Pacific slab beneath southwest Japan with Hi-net receiver functions, *Earth Planet. Sci. Lett.* **239,** 9–17, doi: 10.1016/j.epsl.2005.08.009.

Peacock, S. M. (2009). Thermal and metamorphic environment of subduction zone episodic tremor and slip, *J. Geophys. Res.* **114,** no. B8, doi: 10.1029/2008JB005978.

Peterson, J. (1993). Observations and modelling of seismic background noise, *USGS Open File Report 93-322* doi: 10.3133/ofr93322.

Plourde, A. P., M. G. Bostock, P. Audet, and A. M. Thomas (2015). Low-frequency earthquakes at the southern Cascadia margin, *Geophys. Res. Lett.* **42,** 4849–4855, doi: 10.1002/2015GL064363.

Rubinstein, J. L., M. La Rocca, J. E. Vidale, K. C. Creager, and A. G. Wech (2008). Tidal modulation of nonvolcanic tremor, *Science* **319,** 186–189, doi: 10.1126/science.1150558.

Schmalzle, G. M., R. McCaffrey, and K. C. Creager (2014). Central Cascadia subduction zone creep, *Geochem. Geophys. Geosys.* **15,** 1515–1532, doi: 10.1002/2013GC005172.

Shelly, D. R., G. C. Beroza, S. Ide, and S. Nakamula (2006). Low-frequency earthquakes in Shikoku, Japan, and their relationship to episodic tremor and slip, *Nature* **442,** 188–191, doi: 10.1038/nature04931.

Stanciu, A. C., and E. D. Humphreys (2021). Seismic architecture of the upper mantle underlying California and Nevada, *J. Geophys. Res.* **126,** doi: 10.1029/2021JB021880.

Sweet, J. R., K. R. Anderson, S. Bilek, M. Brudzinski, X. Chen, H. DeShon, C. Hayward, M. Karplus, K. Keranen, C. Langston, *et al.* (2018). A community experiment to record the full seismic wavefield in Oklahoma, *Seismol. Res. Lett.* **89,** 1923–1930, doi: 10.1785/0220180079.

Thomas, A. M., A. Inbal, J. Searcy, D. R. Shelly, and R. Bürgmann (2021). Identification of low-frequency earthquakes on the San Andreas Fault with deep learning, *Geophys. Res. Lett.* **48,** 1–10, doi: 10.1029/2021GL093157.

van Keken, P. E., B. R. Hacker, E. M. Syracuse, and G. A. Abers (2011). Subduction factory: 4. Depth-dependent flux of H_2O from subducting slabs worldwide, *J. Geophys. Res.* **116,** no. B1, doi: 10.1029/2010JB007922.

Wang, Y., F. C. Lin, B. Schmandt, and J. Farrell (2017). Ambient noise tomography across Mount St. Helens using a dense seismic array, *J. Geophys. Res.* **122,** 4492–4508, doi: 10.1002/2016JB013769.

Wang, Y., F. C. Lin, and K. M. Ward (2019). Ambient noise tomography across the Cascadia subduction zone using dense linear seismic arrays and double beamforming, *Geophys. J. Int.* **217,** 1668–1680, doi: 10.1093/gji/ggz109.

Ward, K. M., and F. Lin (2017). On the viability of using autonomous three-component nodal geophones to calculate teleseismic *Ps* receiver functions with an application to old faithful, Yellowstone, *Seismol. Res. Lett.* **88,** 1268–1278, doi: 10.1785/0220170051.

Ward, K. M., F. Lin, and B. Schmandt (2018). High-resolution receiver function imaging across the Cascadia subduction zone using a dense nodal array, *Geophys. Res. Lett.* **45,** 12,218–12,225, doi: 10.1029/2018GL079903.

Wech, A. G. (2010). Interactive tremor monitoring, *Seismol. Res. Lett.* **81,** 664–669, doi: 10.1785/gssrl.81.4.664.

Wessel, P., W. H. F. Smith, R. Scharroo, J. Luis, and F. Wobbe (2013). Generic Mapping Tools: Improved version released, *Eos Trans. AGU* **94,** 409–410, doi: 10.1002/2013EO450001.

Manuscript received 29 July 2022
Published online 7 November 2022